ELECTRON–ION RECOMBINATION OF Mg6+ FORMING Mg5+ AND OF Mg7+ FORMING Mg6+: LABORATORY MEASUREMENTS AND THEORETICAL CALCULATIONS

M. Lestinsky[1,5], N. R. Badnell[2], D. Bernhardt[3], D. Bing[4], M. Grieser[4], M. Hahn[1], J. Hoffmann[4],
B. Jordon-Thaden[4], C. Krantz[4], O. Novotný[1,4], D. A. Orlov[4], R. Repnow[4], A. Shornikov[4], A. Müller[3],
S. Schippers[3], A. Wolf[4], AND D. W. Savin[1]

[1] Columbia Astrophysics Laboratory, Columbia University, New York, NY 10027, USA; m.lestinsky@gsi.de
[2] Department of Physics, University of Strathclyde, Glasgow G4 0NG, UK
[3] Institut für Atom- und Molekülphysik, Justus-Liebig-Universität Giessen, D-35392 Giessen, Germany
[4] Max-Planck-Institut für Kernphysik, D-69117 Heidelberg, Germany

ABSTRACT

We have measured electron–ion recombination for C-like Mg6+ forming Mg5+, and for B-like Mg7+ forming Mg6+. These studies were performed using a merged electron–ion beam arrangement at the TSR heavy ion storage ring located in Heidelberg, Germany. Both primary ions have metastable levels with significant lifetimes. Using a simple cascade model we estimate the population fractions in these metastable levels. For the Mg6+ results, we find that the majority of the stored ions are in a metastable level, while for Mg7+ the metastable fraction is insignificant. We present the Mg6+ merged beams recombination rate coefficient for DR via $N = 2 \rightarrow N' = 2$ core electron excitations ($\Delta N = 0$ DR) and for Mg7+ via $2 \rightarrow 2$ and $2 \rightarrow 3$ core excitations. Taking the estimated metastable populations into account, we compare our results to state-of-the-art multiconfiguration Breit–Pauli theoretical calculations. Significant differences are found at low energies where theory is known to be unreliable. Moreover, for both ions we observe a discrepancy between experiment and theory for $\Delta N = 0$ DR involving capture into high-n Rydberg levels and where the stabilization is primarily due to a radiative transition of the excited core electron. This is consistent with previous DR experiments on M-shell iron ions which were performed at TSR. The large metastable content of the Mg6+ ion beam precludes generating a plasma recombination rate coefficient (PRRC). However, this is not an issue for Mg7+ and we present an experimentally derived Mg7+ PRRC for plasma temperatures from 400 K to 10^7 K with an estimated uncertainty of less than 27% at a 90% confidence level. We also provide a fit to our experimentally derived PRRC for use in plasma modeling codes.

Key words: atomic data – atomic processes

1. INTRODUCTION

Analyzing and modeling spectra of cosmic atomic plasmas requires an accurate understanding of the underlying microphysics that produces the observed spectra. Particularly important are reliable ionization balance calculations for both photoionized and electron-ionized gas (Ferland 2003; Kallman & Palmeri 2007; Bryans et al. 2009). Examples of photoionized plasmas (PPs) include active galactic nuclei, X-ray binaries, cataclysmic variables, cold nova shells, H II regions, and planetary nebulae. Collisionally ionized plasmas (CPs) are formed in the Sun, stars, supernova remnants, the interstellar medium, galaxies, and clusters of galaxies. Modeling and analyzing spectra from both, PP and CP sources requires a reliable calculated charge balance distribution (CSD) for the gas. This in turn hinges on accurate ionization and recombination data. Of the relevant recombination processes determining the CSD of the gas, dielectronic recombination (DR) is generally the most important as it is the dominant electron–ion recombination mechanism for most ions in low density plasmas. DR is an electron–ion interaction with a rich, energy-dependent resonance structure. Motivated by the astrophysical importance of DR, we have carried out a series of experimental studies to generate reliable DR data and plasma recombination rate coefficients for the plasma modeling community (Schippers 2009; Schippers et al. 2010). This paper is a continuation of that work.

DR is a two-step recombination process that begins when a free electron approaches an ion, collisionally excites a bound electron of the ion, and is simultaneously captured into a level with principal quantum number n. The core electron excitation can be labeled $Nl_j \rightarrow N'l'_{j'}$, where N is the principal quantum number of the core electron, l is the orbital angular momentum, and j is its total angular momentum. Conservation of energy for dielectronic capture requires that

$$\Delta E = E_k + E_b, \quad (1)$$

where ΔE is the core excitation energy, E_k is the kinetic energy of the incident electron, and E_b is the binding energy of the captured electron in the core-excited ion. Because ΔE and E_b are quantized, DR is a resonant process. The intermediate state, formed by simultaneous excitation and capture, may autoionize. The DR process is complete when the intermediate state emits a photon which reduces the total energy of the recombined ion to below its ionization limit. See Müller (2008) for additional details.

Here we present experimental and theoretical DR results for Mg6+ forming Mg5+ and for Mg7+ forming Mg6+. These ions are found in many of the cosmic sources listed above. Magnesium is formed with fractional abundances $\geqslant 1\%$ in the 6+ charge state in PPs at electron temperatures T_e in the range of $k_B T_e = 1.1$–3.4 eV (Kallman & Bautista 2001) and in CPs at $k_B T_e = 27$–104 eV (Bryans et al. 2009), where k_B is the Boltzmann constant. Similarly, Mg7+ ions are abundant in photoionized gas at $k_B T_e = 1.25$–11.9 eV (Kallman & Bautista

Table 1
Energy Levels of Mg^{6+} Relative to the $2s^2\, 2p^2\ ^3P_0$ Ground Level
(Ralchenko et al. 2008) for Excitations within the L-shell along with
Their Respective Lifetimes from Our AUTOSTRUCTURE Calculations

Level	Energy (eV)	Lifetime (s)
$2s^2\, 2p^2\ ^3P_1$	0.1373	38.88
$2s^2\, 2p^2\ ^3P_2$	0.3625	12.00
$2s^2\, 2p^2\ ^1D_2$	5.0769	2.04(−1)
$2s^2\, 2p^2\ ^1S_0$	10.558	2.38(−2)
$2s\, 2p^3\ ^5S_2^o$	14.6425	2.27(−5)
$2s\, 2p^3\ ^3D_3^o$	28.8701	5.26(−10)
$2s\, 2p^3\ ^3D_2^o$	28.8830	5.13(−10)
$2s\, 2p^3\ ^3D_1^o$	28.8913	5.06(−10)
$2s\, 2p^3\ ^3P_1^o$	34.0829	1.93(−10)
$2s\, 2p^3\ ^3P_2^o$	34.0837	1.95(−10)
$2s\, 2p^3\ ^3P_0^o$	34.0891	1.02(−10)
$2s\, 2p^3\ ^1D_2^o$	43.9401	6.41(−11)
$2s\, 2p^3\ ^3S_1^o$	44.8968	3.10(−11)
$2s\, 2p^3\ ^1P_1^o$	49.2407	3.86(−11)
$2p^4\ ^3P_2$	67.2386	5.56(−11)
$2p^4\ ^3P_1$	67.4961	5.52(−11)
$2p^4\ ^3P_0$	67.6041	5.51(−11)
$2p^4\ ^1D_2$	71.450	1.10(−10)
$2p^4\ ^1S_0$	81.636	4.67(−11)

Note. The data format $x(y)$ signifies $x \times 10^y$.

2001) and in collisionally ionized gas at $k_B T_e = 36$–125 eV
(Bryans et al. 2009).

We have measured DR in C-like Mg^{6+} in the energy range of
0–55 eV, where resonant structure is formed through the capture
channels

$$Mg^{6+}\,(2s^2\, 2p^2\ ^3P_{\{0,1,2\}}) + e^- \rightarrow \begin{cases} Mg^{5+}\,(2s^2\, 2p^2\ nl) \\ Mg^{5+}\,(2s\, 2p^3\ nl). \end{cases} \quad (2)$$

For B-like Mg^{7+} we have measured DR between 0 and 220 eV.
Here the capture channels are

$$Mg^{7+}\,(2s^2\, 2p\ ^2P_{1/2}) + e^- \rightarrow \begin{cases} Mg^{6+}\,(2s^2\, 2p\ ^2P_{3/2}\ nl) \\ Mg^{6+}\,(2s\, 2p^2\ nl) \\ Mg^{6+}\,(2s\, 2p\ 3l'\ nl) \\ Mg^{6+}\,(2s^2\, 3l'\ nl). \end{cases} \quad (3)$$

The closed K-shell has been omitted above. Throughout the rest
of this paper, we refer to each ion by the initial charge state
of the recombining system. The energies of the core transitions
relative to the ground level for each ion are listed in Tables 1
and 2, respectively.

The rest of this paper is organized as follows. In Section 2,
we summarize the theoretical methods used for the calculated
data. A brief description of the experimental setup is given in
Section 3. We discuss methods for estimating the metastable
fractions in the ion beams in Section 4. In Section 5, the
experimental and theoretical results are given and compared in
Section 6. We review the differences found for high-n Rydberg
levels in the light of evidence for other ions and charge states
in Section 7. Plasma rate coefficients are presented in Section 8
and a summary is given in Section 9.

2. THEORY

2.1. Dielectronic Recombination

Jacobs et al. (1979) published the first detailed DR cal-
culations for Mg^{6+} and Mg^{7+} using a "single configuration

Table 2
Same as Table 1, but for Mg^{7+} Relative to the $2s^2\, 2p\ ^2P_{1/2}^o$ Ground Level
(Ralchenko et al. 2008)

Level	Energy (eV)	Lifetime (s)
$2s^2\, 2p\ ^2P_{3/2}^o$	0.4094	3.231
$2s\, 2p^2\ ^4P_{1/2}$	16.104	6.97(−6)
$2s\, 2p^2\ ^4P_{3/2}$	16.246	5.71(−5)
$2s\, 2p^2\ ^4P_{5/2}$	16.454	1.96(−5)
$2s\, 2p^2\ ^2D_{5/2}$	28.7983	5.27(−10)
$2s\, 2p^2\ ^2D_{3/2}$	28.8024	5.06(−10)
$2s\, 2p^2\ ^2S_{1/2}$	36.7983	1.19(−10)
$2s\, 2p^2\ ^2P_{1/2}$	39.5164	6.42(−11)
$2s\, 2p^2\ ^2P_{3/2}$	39.7646	6.37(−11)
$2p^3\ ^4S_{3/2}$	51.2811	7.19(−11)
$2p^3\ ^2D_{5/2}$	57.7450	2.00(−10)
$2p^3\ ^2D_{3/2}$	57.7541	2.00(−10)
$2p^3\ ^2P_{1/2}^o$	65.0486	8.17(−11)
$2p^3\ ^2P_{3/2}^o$	65.0720	8.21(−11)
$2s^2\, 3s\ ^2S_{1/2}$	150.106	
$2s^2\, 3d\ ^2D_{3/2}$	165.626	
$2s^2\, 3d\ ^2D_{5/2}$	165.647	
$2s\, 2p\, (^3P^o)\, 3s\ ^4P_{1/2}^o$	167.551	
$2s\, 2p\, (^3P^o)\, 3s\ ^4P_{3/2}^o$	167.692	
$2s\, 2p\, (^3P^o)\, 3s\ ^4P_{5/2}^o$	167.943	
$2s\, 2p\, (^3P^o)\, 3s\ ^2P_{5/2}^o$	171.278	
$2s\, 2p\, (^3P^o)\, 3s\ ^2P_{5/2}^o$	171.564	
$2s\, 2p\, (^3P^o)\, 3p\ ^2P_{1/2}$	174.616	
$2s\, 2p\, (^3P^o)\, 3p\ ^2P_{3/2}$	174.743	
$2s\, 2p\, (^3P^o)\, 3p\ ^2D_{3/2}$	178.613	
$2s\, 2p\, (^3P^o)\, 3p\ ^2D_{3/2}$	178.888	

approximation" and considered only LS-allowed excitations
of the core electron in the dielectronic capture process. This
approach, necessitated partly by the limited computational re-
sources of the era, omits the low-energy fine-structure reso-
nance excitations important in photoionized gas. More recently
DR was calculated by Gu (2003) utilizing the Flexible Atomic
Code, a relativistic configuration interaction method using a
distorted wave approximation. Since then, multi-configuration
Breit–Pauli (MCBP) calculations have been published for Mg^{6+}
by Zatsarinny et al. (2004) and for Mg^{7+} by Altun et al. (2004,
2005). Our theoretical work here builds on these MCBP results.
Similarly to the previous calculations, we have adjusted the the-
oretical core transition energies ΔE to the known values from the
NIST atomic database (Ralchenko et al. 2008). Here, the theoret-
ical computations were also optimized specifically for the given
target ions.

We have calculated DR data using an MCBP approach,
implemented within the AUTOSTRUCTURE code (Badnell
1986, 2011). Briefly, the AUTOSTRUCTURE code was used to
calculate energy levels as well as radiative and autoionization
rates in the intermediate coupling approximation. These must be
post-processed to obtain the final-state, level-resolved, and total
DR data. Radiative transitions between autoionizing states were
accounted for in the calculations. The DR cross section was
approximated by the sum of Lorentzian profiles for all included
resonances. The basic description of the initial electron target
for Mg^{6+} includes the $2s^2\, 2p^2$, $2s\, 2p^3$, $2p^4$, $2s^2\, 2p\, 3l$, $2s\, 2p^2\, 3l$,
$2p^3\, 3l$ configurations. For Mg^{7+} the $2s^2\, 2p$, $2s\, 2p^2$, $2p^3$, $2s^2\, 3l$,
$2s\, 2p\, 3l$, and $2p^2\, 3l$ configurations were used. A closed-shell
He-like core is assumed for each ion.

2.2. Radiative Recombination

For each ion we have calculated the non-resonant radiative recombination (RR) both using AUTOSTRUCTURE as well as using a hydrogenic quantum mechanical dipole approximation for low n and a semiclassical approach with Stobbe corrections for high n (Stobbe 1930). For high-n Rydberg levels, we apply corrections to the theoretical cross section to account for field ionization (Schippers et al. 2001). Doing all this yields the RR cross section $\sigma_{\rm theo}^{\rm RR}$ for the AUTOSTRUCTURE results and $\sigma^{\rm RR}$ for the hydrogenic/semiclassical results. Both sets of results are used later in this paper.

3. EXPERIMENTAL METHOD

Measurements were performed in a merged electron–ion beams arrangement at the heavy ion storage ring TSR located at the Max-Planck-Institute for Nuclear Physics (MPIK) in Heidelberg, Germany (Baumann et al. 1988). TSR has a long history of electron–ion collision studies and detailed descriptions of the experimental setup have been given by Kilgus et al. (1992), Lampert et al. (1996), Pastuszka et al. (1996), Schippers et al. (2001), Wolf et al. (2006), and Lestinsky et al. (2009). Here, we give only a brief summary of the setup and a short description of the particulars used for our experimental results.

The ring is equipped with two electron beam devices installed in separate sections. An electron beam can be merged with the circulating ions in each of these sections. The Mg^{6+} and Mg^{7+} data sets were collected using the permanently installed electron beam device (Steck et al. 1990; Pastuszka et al. 1996), commonly referred to as the Cooler. This unit was operated as a probe beam for electron–ion collisions studies at tunable relative energies. We used adiabatic transverse expansion of the electron beam (Pastuszka et al. 1996) with an expansion ratio of $\xi = 9.6$ to decrease the initial transverse velocity spread of the electron beam due to the temperature of the thermionic cathode $k_B T_{\rm cath} \approx 0.13$ eV. The electron beam is parameterized by a flattened double-Maxwellian electron velocity distribution (Kilgus et al. 1992). Fits to the Mg^{7+} data yielded electron beam temperatures of $k_B T_\perp = 13.5(2)$ meV and $k_B T_\parallel = 0.180(5)$ meV, perpendicular and parallel to the electron beam direction, respectively. The uncertainty in the last digit(s) is given by the number in the parentheses. All uncertainties here and throughout the rest of the paper are given at an estimated 90% confidence level. In addition, for Mg^{7+} we also scanned the near-threshold region with an increased expansion factor of $\xi = 23.7$ and a reduced electron current. These steps allowed us to investigate the near-zero DR resonances at a higher resolution. For these data, we derived $k_B T_\perp = 5.4(2)$ meV and $k_B T_\parallel = 0.110(5)$ meV from our fits.

The recombined ions formed in the Cooler were deflected from the parent ion beam in the first downstream dipole magnet of the TSR lattice. We measured these products with a movable scintillation detector (Miersch et al. 1996) used in single particle counting mode with nearly unity efficiency. After the interaction region the recombined ions experience several regions with various magnetic fields: the demerging section of the Cooler, correction and focusing magnets, and one of the main dipoles forming the closed orbit for the stored ions. These magnets induce motional electric fields as seen by the ions, leading to field ionization of high-n Rydberg levels before their arrival at the detector. Any re-ionized ions are deflected off the trajectory to the scintillation detector, and thus not detected. For the magnetic field strengths and ion velocities used here, the

semiclassical value for this field-ionization cutoff (Gallagher 1994) is $n_{\rm cut} = 27$ for Mg^{6+} and $n_{\rm cut} = 32$ for Mg^{7+}. However, some levels of n above $n_{\rm cut}$ can radiatively decay to below $n_{\rm cut}$ during the flight time from the interaction zone through the magnets and are therefore detected. Schippers et al. (2001) have developed a hydrogenic model to derive (n, l)-specific detection probabilities, taking into account the field ionization and radiative de-excitation processes. We use this model when comparing our MCBP results to our experimental data.

The second electron beam device is the ultracold photocathode electron target (Sprenger et al. 2004; Orlov et al. 2005), commonly referred to as the Target. This device was operated as an electron cooler with constant electron velocity matched to the velocity of the ions during the Mg^{6+} data collection. This allowed for continuous electron cooling of the ion beam (Poth 1990). During the Mg^{7+} beam time, the Target was not available for experiments and the Cooler was used to cool the ions, as is described below.

$^{24}Mg^{6+}$ and $^{24}Mg^{7+}$ ions were prepared in the tandem accelerator facility and injected into TSR at energies of $E_{\rm ion} = 77.1$ MeV and 80.1 MeV, respectively, corresponding to ion velocities $\approx 8\%$ of the speed of light. Injection was performed using multi-turn injection and "ecool stacking" (Grieser et al. 1991) with several successive shots, one per second, to maximize the initial ion current. The stored, cooled ion beams had lifetimes of ≈ 19 s and 35 s, respectively. A brief phase of electron cooling followed the injection, during which the electron energy in the Cooler was tuned to match the electron velocity to the ion velocity. Over the active data collection phase typical average ion currents of 14 μA for Mg^{6+} and 12.5 μA for Mg^{7+} were reached.

For data collection the Cooler electron energy was repeatedly stepped through a sequence of two (three) different energies for Mg^{6+} (Mg^{7+}). For Mg^{6+} the electron energy was switched between a measurement energy and a reference energy while cooling was provided by the Target. Since the Target was unavailable for the Mg^{7+} work, ion beam cooling had to be provided by the Cooler in this case. Thus, the measurement scheme was extended by adding a cooling step before each measurement and reference pair. Typically, data were collected for 500 pairs of steps for Mg^{6+} and for 1450 sets for Mg^{7+}. The measurement energy was incremented in the laboratory frame by a variable $\Delta E_{\rm lab}$ between steps. Depending on the relative energy and the richness of the observed structure, $\Delta E_{\rm lab}$ was varied between 0.153 and 1.53 eV for Mg^{6+} and between 0.244 and 0.457 eV for Mg^{7+}. The reference-step energy was chosen to lie at an energy where the observed data showed no significant electron–ion recombination signal and the background is largely due to electron capture collisions of ions with residual gas particles in TSR.

4. METASTABLE POPULATIONS

Using a metal–ion sputter source, a beam of MgH_2^- was produced and injected into the tandem accelerator. The ions were then accelerated toward a positively biased diamond-like carbon foil ($U_{\rm foil} \approx 10$ MV). Passing through the foil broke up the molecules and the resulting Mg ions underwent multiple electron stripping and capture collisions with foil electrons. The charge state of the stripped Mg ions is a function of the ion energy in the stripping foil (Shima et al. 1992). Using magnetic dipole fields, the desired charge state of either $q = 6+$ or $7+$ was separated from the remainder of this distribution and injected into TSR.

A consequence of the randomness of this ion production method is that the ions can be essentially in any excited state upon exiting the stripping foil. In fact, this method of ion generation has been used in beam foil spectroscopy for a long time for highly charged ions to study excited states and their lifetimes (Martinson & Gaupp 1974; Träbert et al. 2009). For a quantitative analysis of our experimental data, we need to determine the population of each metastable level during the measurement. To this end, we have developed an approach which follows the decay cascade as a function of storage time. The change in the level i population $\mathcal{P}_i$ is given by the differential equation

$$\frac{d\mathcal{P}_i}{dt} = -\sum_{j<i} \mathcal{P}_i A_{ij} + \sum_{k>i} \mathcal{P}_k A_{ki}, \qquad (4)$$

where j and k denote, respectively, levels lying below and above i in energy and the A terms are the radiative rates. The first term on the right-hand side of Equation (4) accounts for losses from level i into any lower levels j. The second term gives the feeding contributions from decays of any higher channel k into level i.

We solve Equation (4) numerically. The initial population $\mathcal{P}_i(t_0 = 0)$ for each level i is deduced from a statistically weighted Boltzmann distribution. As an estimate for the temperature of this distribution we assume that the stripping process is dominated by the collisions of the ions with the foil electrons. The kinetic energy of the MgH$_2^-$ is $E_{\rm ion} = 10$ MeV. The collision energy of the electrons, as seen by the rest frame of the ions, is then $E_e = (m_e/m_{\rm ion})E_{\rm ion} \approx 210$ eV, where m_e is the electron mass and $m_{\rm ion}$ is the MgH$_2^-$ mass. We take this effective electron energy to be the temperature $k_B T_e$ of the Boltzmann distribution describing the initial population of levels in the final charge state of the stripped ion for both Mg^{6+} and Mg^{7+}. Using AUTOSTRUCTURE (Badnell et al. 2003), we have calculated the Einstein A_{ij} rates for radiative decays within the L-shell, considering all important electric and magnetic multipole orders of these transitions. Since the dynamic range of the decay channels A_{ij} spans up to 15 orders of magnitude for the transitions covered here, we use exponentially increasing step sizes for the time steps t_n to keep the computations tractable. Furthermore, we have to restrict these calculations onto a compact set of possible excited levels i and make plausible assumptions for the contributions from those levels omitted. In a simple scenario we include only excited levels within the L-shell. For Mg^{6+}, there are 20 such levels. For Mg^{7+}, one finds 15 such levels (Ralchenko et al. 2008). In an extended second scenario for Mg^{6+} we also include all excited levels within the M-shell giving a total of 236 levels. Between both scenarios for Mg^{6+} we find a relative change of less than $\pm6\%$ in the final population of each level. Therefore, we assume that cascades from higher levels are unimportant and we include only L-shell excitations for the computations below.

4.1. Mg^{6+} Metastable Population

Mg^{6+} has several long-lived metastable levels: the $2s^2\,2p^2\,{}^3P_{\{1,2\}}$, ${}^1D_2$, and ${}^1S_0$ levels and the $2s\,2p^3\,{}^5S_2^o$ level, the lifetimes of which are given in Table 1. These populations are considerably long-lived in the context of this experiment and have complex decay chains.

Utilizing the model described above, we have performed an analysis of the metastable populations, taking into account the specific injection and cooling times in a typical measurement scenario. The results are given in Figure 1 for a singular injection burst and in Figure 2 with ecool stacking (see Section 3). Both

Table 3
Time-averaged Mg^{6+} Metastable Population Fractions $\langle\mathcal{P}_i^{\rm casc}\rangle$ for the Conditions of Our Experiment (see Section 4)

Level	i	$\langle\mathcal{P}_i^{\rm casc}\rangle$
${}^3P_0$	0	0.244
${}^3P_1$	1	0.588
${}^3P_2$	2	0.168
${}^1D_2$	3	0
${}^1S_0$	4	0
${}^5S_2$	5	0

figures show the evolution of the populations of the metastable levels and the ground state from the moment of the last injection as a function of storage time.

The single-shot results in Figure 1 show the fast relaxations which initially predominantly populate the metastable levels. The multiple bursts of the ecool stacking injection sequence provide the majority of the ion beam with several seconds time to radiatively relax, initially primarily to the long-lived metastable levels. This is shown in Figure 2. After 1 ns, all levels with E1 transitions to lower lying levels have decayed and all ions are in either the ground level or one of the five metastable levels. Within 100 μs the ${}^5S_2$ level has decayed, favoring mostly the ${}^3P_2$ level and to a lesser extent the ${}^3P_1$. At 0.1 s after injection, the ${}^1S_0$ level is mostly gone, followed by the ${}^1D_2$ level at 1 s. Both levels favor decay into the ${}^3P_2$. At 1 s after injection, only the ${}^3P_{\{0,1,2\}}$ levels survive in significant amounts. Out of these, the ${}^3P_2$ level, is initially the dominant fraction for the first 0.6 s with a peak population after 0.3 s where it constitutes 46% of the ion beam. After this, it decays predominantly into the ${}^3P_1$ level which from now on becomes the dominant fraction in the ion beam until approximately 30 s after injection. It reaches its maximum at 12 s storage time, where it makes up 60% of the ion beam. Only after about 30 s of storage does the ${}^3P_0$ ground level become the dominant fraction in the ion beam.

The ion beam storage lifetime and the required times for electron cooling set practical limits to the usable time windows for the experiment. Measurements were carried out with ecool stacking and timed such that the total measurement cycle spanned from 4 to 19 s of storage time. Considering the time range of the active data collection phase, we derive from this model time-averaged population fractions $\langle\mathcal{P}_i^{\rm casc}\rangle$ for each metastable level. These are given in Table 3.

4.2. Mg^{7+} Metastable Population

The Mg^{7+} ion has $2s^2\,2p\;{}^2P_{3/2}^o$ and $2s\,2p^2\;{}^4P_{\{1/2,\,3/2,\,5/2\}}$ metastable levels. The lifetimes of the L-shell levels are listed in Table 2. Using an analysis similar to that for Mg^{6+} above, we find that only a small fraction of the ion beam remains in a metastable level after 3 s of storage time. We estimate that on average 97% of the ion beam is in the ground level during the measurement phase of the experiment.

5. MERGED BEAMS RECOMBINATION RATE COEFFICIENTS

5.1. Experiment

The experiment measures the DR cross section times the relative velocity between the beams convolved with the energy spread of the experiment. We call this the merged beams recombination rate coefficient (MBRRC) to distinguish it from
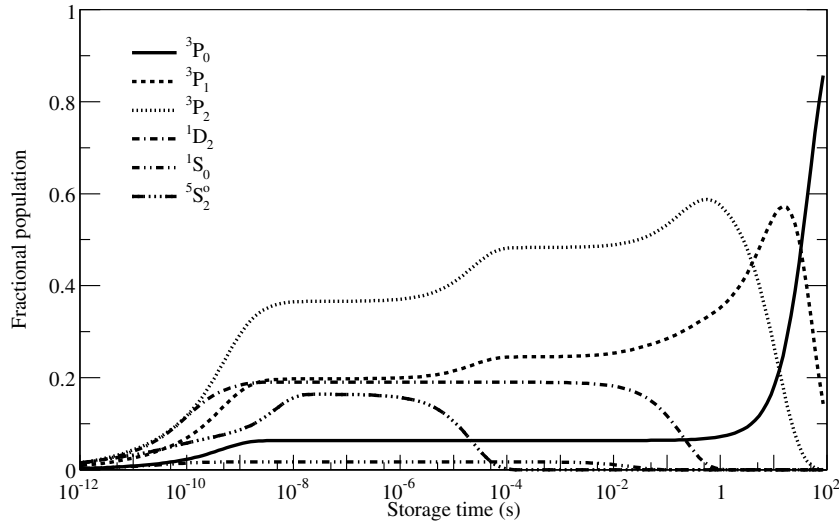
Figure 1. Evolution of the population fractions in Mg^{6+} as a function of the time after the charge state is formed by stripping. All possible L-shell levels were considered, but only the metastable levels and the ground state are shown. The model used here shows the results for one singular ion-injection burst into TSR.
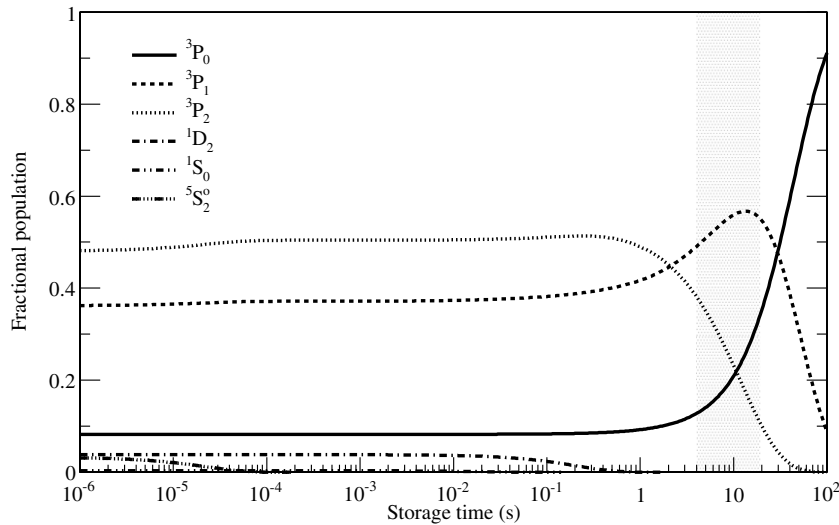

Figure 2. Same as Figure 1, but here the model is for a sequence of multiple injections with ecool stacking as was used for the experiment (see the text). The starting time $t = 0$ corresponds to the end of the injection sequence. The shaded area indicates the time range during which data were collected.

a Maxwellian plasma recombination rate coefficient (PRRC). Figures 3 and 4, respectively, show the experimentally obtained RR+DR MBRRC α_{exp} for Mg^{6+} and Mg^{7+} as a function of collision energy (solid black curves). The experimental energy scale was adjusted to match the theoretical data which in turn are referenced to the core excitation energies from the NIST atomic data base (Ralchenko et al. 2008). For Mg^{6+}, the experimental energy scaling factor was 1. For Mg^{7+} we used a scaling factor of 0.9903. The data reduction methods for deriving an experimental MBRRC have been discussed elsewhere in detail (Schippers et al. 2001, 2004; Schmidt et al. 2006; Lukić et al. 2007; Lestinsky et al. 2008). The total experimental uncertainty for the absolute MBRRC is estimated to be ±25% at a 90% confidence level, due primarily to the ion current calibration (Lampert et al. 1996).

Vertical lines are used in Figures 3 and 4 to indicate the energy position of resonances from the dominant Rydberg series. These resonance energy sequences have been calculated up to n_{cut} for all but the Mg^{7+} $2s^2\,2p\,^2P^o_{3/2}$ nl series where the observed resonances all lie above n_{cut}. The energies are given

by Equation (1), which in a hydrogenic approximation can be rewritten as

$$E_n = \Delta E - \left(\frac{q}{n}\right)^2 \mathcal{R}, \qquad (5)$$

where E_n is the resonance energy for DR into a given n level, q is the charge of the ion before DR, and $\mathcal{R} = 13.6057$ eV is the Rydberg energy. A final line is drawn at the energy position of the $n \to \infty$ limit. The series limits ΔE for each of the respective series were taken from Tables 1 and 2, respectively, and are labeled by the corresponding core excitation level.

5.2. Theory

We have calculated the theoretical RR and DR cross sections for each ion using AUTOSTRUCTURE as described in Section 2 and the field-ionization corrections of Schippers et al. (2001). For each ion both the RR and DR cross sections are convolved with the relative velocity times the experimental electron energy spread (see Section 3) giving the RR MBRRC $\alpha^{\mathrm{RR}}_{\mathrm{theo}}$ and that for DR $\alpha^{\mathrm{DR}}_{\mathrm{theo}}$. The former is shown for each ion using a dotted line in Figures 3 and 4. The total theoretical RR+DR

Figure 3. $Mg^{6+} + e^- \rightarrow Mg^{5+}$ MBRRC as a function of relative energy. The experimental data are shown by the solid black curve. Our AUTOSTRUCTURE calculations are shown by the solid red line. These theoretical results include field ionization and were weighted by the metastable population fractions from the cascade model. The thin dotted line gives the calculated non-resonant RR signal. The upper panel expands the low energy region from 5×10^{-5} to 5 eV in a double logarithmic plot. The lower panel shows the full data from 0 to 55 eV, covering all prominent $\Delta N = 0$ series using linear axes. Vertical lines indicate the dominant DR Rydberg series and are labeled by the corresponding core excitation. See the text for details.

MBRRC for each ion is shown using red curves. For Mg^{6+}, the theoretical DR data were calculated for the initial ground and metastable ^3P_J levels which are expected to contribute to the observed DR spectrum (see Section 4.1). RR is expected to be mostly insensitive to fine-structure-excited metastable levels and the same data are used for all levels considered. Here, we weigh the contributions from each initial level by the population fractions $\langle \mathcal{P}_i \rangle$ derived from our cascade model and show the summed theoretical MBRRC from all initial levels using a solid red curve. For Mg^{7+}, the metastable population fraction is insignificant; hence, we use only the MCBP results for the ground level.

6. COMPARISON BETWEEN EXPERIMENT AND THEORY

6.1. Mg^{6+}

In the near-zero range of $E_k \lesssim k_B T_\perp \approx 13.5$ meV, the experimental MBRRC is enhanced over theory. This enhancement grows with decreasing energy to a factor of approximately 17 at 5×10^{-5} eV. A factor of $\sim$1.5–3 is expected due to an experimental artifact (Gwinner et al. 2000; Wolf & Gwinner 2003; Hörndl et al. 2006). The remaining factor of $\sim$5.6–11.3 suggests the presence of unresolved near-zero eV DR resonances as has been seen for other systems (Uwira et al. 1997; Savin et al. 2002b, 2003; Schmidt et al. 2006; Lestinsky et al. 2009; Schippers et al. 2011).

One might be tempted to attribute these unresolved resonances to DR series associated with core excitations between the $2s^2 \, 2p \, ^3P_J$ levels. But, energetically, the lowest possible n levels are $n = 37$ for the $^3P_0 \rightarrow ^3P_2$ core excitation, $n = 47$ for the $^3P_1 \rightarrow ^3P_2$ core excitation, and $n = 60$ for the $^3P_0 \rightarrow ^3P_1$

core excitation. These are unlikely to be the sources of the difference. When one takes into account the interplay of field ionization with the radiative stabilization of these levels from cascades, we find l-averaged detection probabilities of <0.1%.

Astrophysically, the observed near-zero eV resonances are unlikely to be important. They lie at energies below $\approx$0.013 eV. Hence, their contributions are insignificant to the PRRC for DR of Mg^{6+} which forms at plasma temperatures (in eV) several orders of magnitude higher.

From 0.013 to 0.5 eV, experiment and theory show significant differences in both the DR resonance structure and strength. Theory does not well reproduce either the measured resonance structure or the integrated strength. In order to quantify the differences in resonance strength between theory and experiment, we define

$$\kappa = \frac{\int \alpha_{\text{theo}}^{\text{DR}} \, dE}{\int \alpha_{\text{exp}}^{\text{DR}} \, dE} \tag{6}$$

with $\alpha_{\text{exp}}^{\text{DR}} = \alpha_{\text{exp}} - \alpha_{\text{theo}}^{\text{RR}}$. We find $\kappa = 0.673(16)$ for this energy range (see also Table 4). Here and throughout the remainder of this section, the uncertainty given in parentheses includes only the statistical errors at a 90% confidence level. The agreement improves somewhat between 0.5 and 1.1 eV with fewer deviations seen in the DR structure and a $\kappa = 0.894(13)$. Between 1.1 and 4 eV lies a group of DR resonances that we assign to $2s \, 2p^3 \, ^3P_J^0 \, 4l$ configurations. Here, the agreement continues to improve in both the resonance structure and integrated resonance strength with $\kappa = 1.114(9)$.

The experimental data between 4 and 46 eV show three prominent DR Rydberg series which can be attributed to core excitations of the $2s \, 2p^3 \, ^3D_{\{3,2,1\}}$, $^3P_{\{1,2,0\}}$, and $^3S_1^o$ levels. Individual features can be assigned to Rydberg levels starting
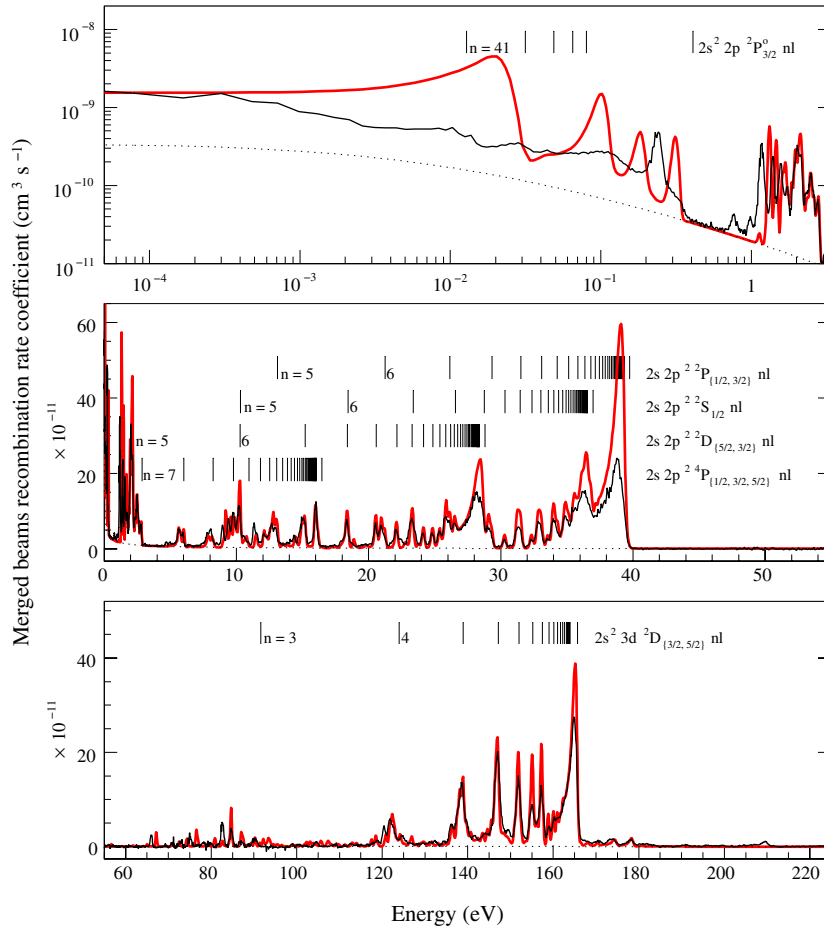
Figure 4. Same as Figure 3, but for $Mg^{7+} + e^- \rightarrow Mg^{6+}$.

Table 4
Comparison of the Mg^{6+} Theoretical DR MBRRC, Summing Ground State
and Metastable Levels Weighted by $\langle \mathcal{P}_i^{casc} \rangle$, with Our Experimental Data

Energy Interval (eV)	$\int \alpha_{theo}^{DR} dE$	$\int \alpha_{exp}^{DR} dE$ (10^{-10} cm^3 s^{-1} eV)	κ
0.013–0.5	0.274	0.407(6)	0.673(16)
0.5–1.1	0.314	0.351(3)	0.894(13)
1.1–4	0.872	0.783(4)	1.114(9)
4–17	1.572	1.409(6)	1.116(8)
17–25.5	1.397	1.394(4)	1.002(5)
25.5–29.5	2.511	2.472(4)	1.015(3)
29.5–32	0.901	0.769(1)	1.172(2)
32–34	1.800	1.422(1)	1.266(2)
34–43	2.443	1.875(2)	1.303(2)
43–46	2.783	2.269(1)	1.226(1)

Notes. In order to compare only the DR component of the spectrum we have subtracted the calculated RR contributions from our experimental data. The given errors are purely statistical and give the 90% confidence interval.

from $n = 4$ or $n = 5$ going up to about $n = 14$. After this the features blend into one another, forming the characteristic $n \rightarrow \infty$ DR series limit cusps at about 28, 33, and 44 eV, respectively. For the energy ranges up to and including the first cusp at 28 eV, we find good agreement between the integrated experimental and theoretical DR MBRRC, to within the total experimental uncertainty limits. In particular, from 4 to 17 eV we find $\kappa = 1.116(8)$; from 17 to 25.5 eV, $\kappa = 1.002(5)$; and

from 25.5 to 29.5 eV, $\kappa = 1.015(3)$. Above the ^3D_J series limits we find larger differences with theory, with $\kappa = 1.172(2)$ from 29.5 to 32 eV, $\kappa = 1.266(2)$ from 32 to 34 eV, $\kappa = 1.303(2)$ from 34 to 43 eV, and $\kappa = 1.226(1)$ from 43 to 46 eV. Table 4 summarize all the κ results for Mg^{6+}.

6.2. Mg^{7+}

In the near-zero range of $E_k \lesssim k_B T_\perp \approx 13.5$ meV, the experimental MBRRC is enhanced over the sum of RR calculations and modeled DR data (see below). Their ratio reaches up to a factor of 1.75 at 5×10^{-5} eV, which is within the usual range of ~ 1.5–3 expected in the absence of unresolved DR resonances near-zero eV. Theory does predict a strong resonance at ≈ 20 meV which when included brings theory and experiment into agreement at 5×10^{-5} eV due to the extended low-energy tail of its asymmetric MBRRC resonance shape when convolved with the electron beam temperatures. However, no such resonances can be identified in the experimental data, and hence, this agreement seems fortuitous.

From 13.5 meV to 0.41 eV, we find significant differences between theory and experiment. Most evident is that theory predicts four strong DR resonances with peak energies of ≈ 0.02, 0.1, 0.18, and 0.3 eV due to dielectronic capture into the $2s\,2p^2$ ^2D $5p$ levels. However, experiment shows only one strong resonance at ≈ 0.25 eV, which cannot be unambiguously attributed to any particular level. These differences likely arise from an overestimate of the theoretical energies for these double excited levels in the recombined ion.
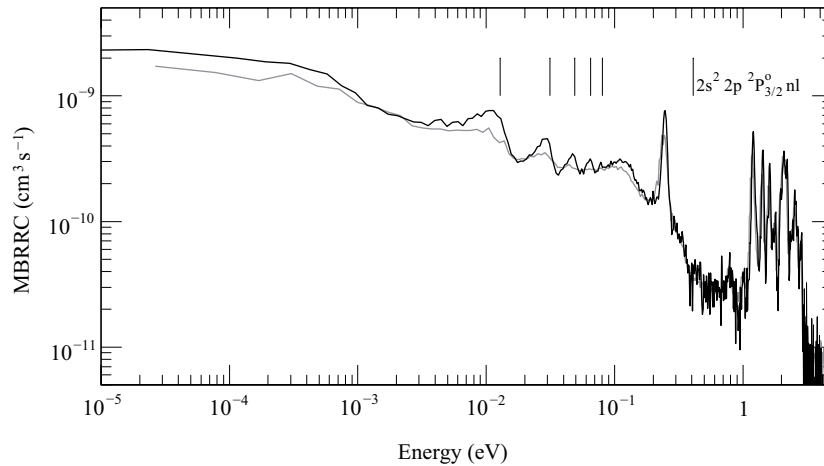
7

Figure 5. Comparison of the experimental Mg^{7+} MBRRC for two different sets of electron beam temperatures. The data shown with a black curve is for the "high-expansion" electron beam, whereas the gray curve shows the data for the "high-density" electron beam parameters from Figure 4 (see the text). Analysis of peak shapes yields electron temperatures of $k_B T_\perp = 5.4(1)$ meV and $k_B T_\parallel = 0.110(5)$ meV for the high-expansion data, whereas the high-density data give $k_B T_\perp = 13.5(2)$ meV and $k_B T_\parallel = 0.180(5)$ meV. The sequence of vertical lines indicates selected $2s^2\, 2p\, ^2P_{3/2}\, nl$ resonance positions with $n = 41$–45 and ∞ resulting from Equation (5).

It is interesting to note that between ~ 0.01 and 0.41 eV we see structure which can be attributed to DR via the fine-structure core excitation $2s^2\, 2p\, ^2P^o_{3/2}\, nl$ series, where $n \geqslant 41$. Such levels are above the field-ionization cutoff $n_{\text{cut}} = 32$. However, taking into account the cascading probabilities of such high Rydberg levels (Schippers et al. 2001) still give l-averaged detection probabilities of 6% for $n = 41$ decreasing to 1% for $n = 60$. These detection probabilities are much larger than those for Mg^{6+} due to the lower dipole magnet field strengths in the TSR lattice needed for the more highly charged Mg^{7+}, resulting in a lower motional electric field, and also due to the q^4 dependence for the radiative rate out of Rydberg levels (Marxer & Spruch 1991).

In order to study DR for this series in more detail, we scanned the energy interval below 4 eV with a higher expansion $\xi = 23.7$ and three times lower electron density. This reduced the Cooler electron velocity spread. These data are shown in Figure 5 where we also plot the experimental data from Figure 4 for comparison. We can readily identify DR via capture into Rydberg levels $n = 41, 42, 43,$ and 44. Fitting the energy positions of these resonances gives $0.0130(5)$ eV, $0.0312(8)$ eV, $0.050(1)$ eV, and $0.067(1)$ eV, respectively. As a test of the accuracy of the experimental energy scale, using these and the simple Rydberg formula Equation (5), we derive for the term energy $E(^2P^o_{3/2}) = 0.4097(6)$. This result is in excellent agreement with the value of 0.4094 eV as given in the NIST reference table (Ralchenko et al. 2008).

Between 0.41 to ≈ 0.7 eV, the observed MBRRC is dominated by RR, which agrees well with theory. From ≈ 0.7 eV to 5 eV lies a series of resonances which we attribute to a mixture of $2s\, 2p^2\, ^2D\, 5l$ and $2s\, 2p^2\, ^4P\, 7l$ resonances. At the lower energy end of this range, the measured resonances are found below the energies predicted by theory. This may be related to the overestimate in the resonance energies noted above. At the higher energy of this range, theory and experiment are in good agreement. For this range we find $\kappa = 1.084(6)$. All κ results for Mg^{7+} are listed in Table 5.

In the range of 5–8.5 eV, traces of the $2s\, 2p^2\, ^4P\, nl$ Rydberg series for $n = 8$ and $n = 9$ can be identified at ≈ 6 and ≈ 8 eV, respectively. Other features from this series are not clearly identifiable, as they are expected in energy regions

Table 5
Same as Table 4 but for Ground State Mg^{7+}

Energy Interval (eV)	$\int \alpha^{DR}_{theo}\, dE$ (10^{-10} cm^3 s^{-1} eV)	$\int \alpha^{DR}_{exp}\, dE$	κ
0.013–0.7	1.271	0.515(11)	2.46(5)
0.7–5	2.179	2.011(11)	1.084(6)
5–20	3.368	3.925(7)	0.865(2)
20–27	2.565	2.556(18)	1.004(7)
27–30	2.816	2.103(21)	1.34(1)*
30–37	5.377	3.931(15)	1.368(5)*
37–40	7.165	3.665(13)	1.954(7)*
65–95	1.780	1.63(2)	1.093(13)
95–134	2.787	2.83(1)	0.984(3)
134–143	3.521	3.897(5)	0.904(1)
143–150	3.921	4.347(5)	0.902(2)
150–153.5	2.154	2.165(3)	0.995(1)
153.5–156	1.885	1.321(3)	1.427(3)*
156–158	1.878	1.567(2)	1.198(2)
158–167	9.784	8.565(5)	1.142(2)

Note. * The κ-values marked here are for high-n DR resonances and are above our experimental uncertainty limits.

which are densely populated by DR features from higher lying series. Above 8.5 eV, four prominent DR Rydberg series can be identified, forming characteristic $n \to \infty$ cusps at 28, 36, 39, and 165 eV. These series are attributed, respectively, to the $2s\, 2p^2\, ^2D_{\{5/2, 3/2\}}$, $^2S_{1/2}$, and $^2P_{\{1/2, 3/2\}}$ core excitations for the series limits below 40 eV and to the $2s^2\, 3d\, ^2D_{\{3/2, 5/2\}}$ core excitation for the higher energies.

From 5 eV to 27 eV, the relative line structure and energy positions of the measured DR resonance structure agree well with theory. The absolute DR strengths show good agreement with $\kappa = 0.865(2)$ from 5 to 20 eV and $\kappa = 1.004(7)$ from 20 to 27 eV. However, significant differences are seen at higher energies with $\kappa = 1.34(1)$ for the range of 27–30 eV covering the $^2D_{\{3/2, 5/2\}}$-cusp, 1.368(5) for the range of 30–37 eV spanning the $^2S_{1/2}$-cusp, and 1.954(7) for 37–40 eV range encompassing the $^2P_{\{1/2, 3/2\}}$-cusp.

We also measured $\Delta N = 1$ DR resonances associated with $N = 2 \rightarrow 3$ excitation. These are found in the collision energy range from 60 to 210 eV. The energy scale of the experimental $\Delta N = 1$ spectrum here was calibrated by fitting the measured data to the theoretical results which in turn are referenced to the core excitation energies from NIST atomic database (Ralchenko et al. 2008), requiring first a shift in the experimental energy of 0.29(2) eV followed by the multiplication of the energy scale by a factor of 1.0094(1). The dominant $\Delta N = 1$ DR channel is through $2p \rightarrow 3d$ excitation forming $2s^2\,3d\,^2D\,nl$ resonances with an $n \rightarrow \infty$ series limit at $\Delta E \approx 165.5$ eV.

DR resonances associated with this $\Delta N = 1$ series can be individually resolved and roughly assigned to specific Rydberg levels from $n = 3$ to 9 with capture into higher n levels forming the typical $n \rightarrow \infty$ cusp. A comparison of the integrated strengths from the calculated and experimental MBRRC in general yields reasonable agreement, to within our systematic uncertainty limits. For the $n = 3$ resonances between 65 and 95 eV we find $\kappa = 1.093(13)$. The $n = 4$ resonances between 95 and 134 eV yield $\kappa = 0.984(3)$. For $n = 5$ between 134 and 143 eV, $\kappa = 0.904(1)$. Between 143 and 150 eV ($n = 6$), $\kappa = 0.902(2)$. The $n = 7$ resonances (150–153.5 eV) give $\kappa = 0.995(1)$. Between 153.5 and 156 eV ($n = 8$), we find $\kappa = 1.427(3)$. For $n = 9$ (156–158 eV), $\kappa = 1.198(2)$. Lastly, for $n \geqslant 10$ (158–167 eV), we find $\kappa = 1.142(2)$. Table 5 provides a comprehensive overview over the comparison between experimental and theoretical MBRRC.

7. DISCUSSION OF HIGH-n DR VIA $\Delta N = 0$ CORE EXCITATIONS

The results for Mg^{6+} and Mg^{7+} presented here, taken together with previous storage ring results (which will be referred to below), suggest that a systematic discrepancy may exist between theory and experiment for $\Delta N = 0$ DR resonances where the Rydberg electron occupies $n \gtrsim 10$ and where the radiative stabilization is primarily due to a transition of the excited core electron. One expects the derived κ values to vary within a range of 0.80–1.33. This is due to the typical experimental systematic uncertainty of 25%, dominated by ion current measurements which are independent of the collision energy. However, for these resonances, ratios of $\kappa > 1.33$ are commonly found. To better characterize this discrepancy, we summarize below the relevant previous storage ring measurements for $\Delta N = 0$ DR which have been compared to state-of-the-art theoretical calculations in the energy ranges of these high-n Rydberg resonances (see also Table 6).

Good agreement has been found between theory and experiment for Li- and Na-like ions with $2s$ and $3s$ valence shell configurations, respectively. Similar agreement also exists where the same system has been studied at different facilities. Li-like systems measured include C^{3+} (Schippers et al. 2001) and Cu^{26+} (Kilgus et al. 1992) using the TSR Cooler, and Be^+ (Mohamed et al. 2002), N^{4+} (Böhm et al. 2005), O^{5+} (Böhm et al. 2003), and Ne^{7+} (Böhm et al. 2005) at CRYRING. Experimental work on Na-like Si^{3+} has been performed at CRYRING (Orban et al. 2006) and at the TSR Target (Schmidt et al. 2007). Data are available from CRYRING measurements for Na-like S^{5+} and Ar^{7+} (Orban et al. 2009a, 2009b) Further Na-like studies have been made using the TSR Cooler for Cl^{6+}, Fe^{15+}, and Se^{23+} (Linkemann 1995; Linkemann et al. 1995). Agreement between theory and experiment for almost all these systems lies within the expected range of $0.80 \leqslant \kappa \leqslant 1.33$. The sole exception is

Be^+ with $\kappa = 1.7$; however, the $n_{cut} \approx 7$ for these data render them of little relevance to the present discussion which is for resonances with $n \gtrsim 10$.

Measurements for Be- and Mg-like ns^2 systems with $n = 2$ and $n = 3$, respectively, can be complicated by the presence of long-lived $nsnp\,^3P_0$ metastable levels in the stored ion beam. Some experiments estimate the metastable fraction by comparing the measured and calculated DR resonance cusp at the $\Delta N = 0$ series limit and scale up the measured data to match theory there. This procedure may erroneously eliminate any signature of the high-n discrepancy (e.g., Fogle et al. 2005; Orban et al. 2008, 2010). For some Be-like systems, the metastable compositions were determined by other means with uncertainties commonly well below the typical uncertainties of ~25% for DR MBRRC at a 90% confidence level. For these systems, DR has been studied at TSR for Mg^{8+} (Schippers et al. 2004) and Fe^{22+} (Savin et al. 2006). While good agreement was found between theory and experiment in the case of Fe^{22+}, a $\kappa \approx 1.43$ was found for Mg^{8+}. For Mg-like systems, Fe^{14+} has been studied with the TSR Target and $\kappa \approx 1.31$ was found (Lukić et al. 2007).

Experimental studies of B- and Al-like ns^2np systems have been performed for B-like Fe^{21+} (Savin et al. 2003) and Al-like Fe^{13+} (Schmidt et al. 2006; Badnell 2006a) using the TSR Cooler. In both cases, good agreement was found between theory and experiment for $\Delta N = 0$ DR.

We are aware of very few experimental results for either C- and Si-like ns^2np^2 systems or N- and P-like ns^2np^3 systems. C-like Fe^{20+} (Savin et al. 2003) and N-like Fe^{19+} (Savin et al. 2002b) have been measured using the TSR Cooler. No significant difference between theory and experiment was seen for the relevant high-n DR resonances. However, for P-like Fe^{11+}, a κ of greater than 1.4 was found (Novotný et al. 2012). Data are currently under analysis for Si-like Fe^{12+}.

Moving on to O- and S-like ns^2np^4 valence shell systems, TSR Cooler results exist for O-like Fe^{18+} (Savin et al. 1999, 2002a) and TSR Target results for S-like Fe^{10+} (Lestinsky et al. 2009). While good agreement between theory and experiment exists for Fe^{18+}, one of the largest differences ever found exists for Fe^{10+} with $\kappa \approx 2$.

Few measurements exist for F- and Cl-like $ns^2\,np^5$ systems. TSR Cooler data exist for F-like Fe^{17+} (Savin et al. 1997, 1999) and TSR Target results for Cl-like Fe^{9+} (Lestinsky et al. 2009). Good agreement between theory and experiment is found for Fe^{17+} but not for Fe^{9+} where $\kappa \approx 1.45$.

The last systems we consider here are of the Ar-like ns^2np^6 and K-like ns^2np^6nd type. TSR Cooler results exist for Ar-like Ti^{4+} (Schippers et al. 1998) and Target data for Fe^{8+} (Schmidt et al. 2008). For Ti^{4+}, Nikolić et al. (2009) find a $\kappa \approx 1.42$ for $8 \lesssim n \lesssim 13$. For Fe^{8+}, experiment and theory were found to be in good agreement. However, for K-like Fe^{7+} (Schmidt et al. 2008), a marginal disagreement was found with $\kappa \approx 1.37$.

Table 6 summarizes these findings. It appears that theory and experiment are consistently in good agreement only for ns valence shell systems. For more complicated systems, good agreement is usually found for L-shell systems with charge $q \gtrsim 17$. However, for the lower charged L-shell and M-shell systems measured, more often than not κ is larger than can be explained by the experimental uncertainty. The fact that κ for these systems is always larger than 1 and does not show the scatter seen for the ns systems lends support to the hypothesis that there is an unidentified systematic dependency at work here.

Table 6
A Summary of the DR $\Delta N = 0$ κ Discrepancy for Capture into High-n Levels where $n \gtrsim 10$
and the Stabilization is Primarily Due to a Radiative Decay of the Excited Core Electron

Ion	Initial Configuration	Intermediate Configuration	κ	Reference
		Li- and Na-like		
Be^+	$2s$	$2p\,nl$	1.7	Mohamed et al. (2002)
C^{3+}	$2s$	$2p\,nl$	1.25	Schippers et al. (2001)
N^{4+}	$2s$	$2p\,nl$	0.87	Böhm et al. (2005)
O^{5+}	$2s$	$2p\,nl$	1.25	Böhm et al. (2003)
Cu^{26+}	$2s$	$2p\,nl$	1.1	Kilgus et al. (1992)
Si^{3+}	$3s$	$3p\,nl$	0.88	Schmidt et al. (2007)
S^{5+}	$3s$	$3p\,nl$	1.25	Orban et al. (2009a, 2009b)
Ar^{7+}	$3s$	$3p\,nl$	1.25	Orban et al. (2009a, 2009b)
Fe^{15+}	$3s$	$3p\,nl$	0.94	Linkemann (1995), Linkemann et al. (1995)
Se^{23+}	$3s$	$3p\,nl$	0.94	Linkemann (1995)
		Be- and Mg-like		
Mg^{8+}	$2s^2$	$2s\,2p\,nl$	1.43	Schippers et al. (2004)
Fe^{22+}	$2s^2$	$2s\,2p\,nl$	1	Savin et al. (2006)
Fe^{14+}	$3s^2$	$3s\,3p\,nl$	1.31	Lukić et al. (2007)
		B- and Al-like		
Mg^{7+}	$2s^2\,2p$	$2s\,2p^2\,nl$	1.37	Table 5
Fe^{21+}	$2s^2\,2p$	$2s\,2p^2\,nl$	0.99	Savin et al. (2003)
Fe^{13+}	$3s^2\,3p$	$3s^2\,3d\,nl$	1.18	Badnell (2006a)
		C-like		
Mg^{6+}	$2s^2\,2p^2$	$2s\,2p^3\,nl$	1.32	Table 4
Fe^{20+}	$2s^2\,2p^2$	$2s\,2p^3\,nl$	1.08	Savin et al. (2003)
		N- and P-like		
Fe^{19+}	$2s^2\,2p^3$		0.98	Savin et al. (2002b)
Fe^{11+}	$3s^2\,3p^3$	$3s^2\,3p^2\,3d\,nl$	1.40	Novotný et al. (2012)
		O- and S-like		
Fe^{18+}	$2s^2\,2p^4$	$2s\,2p^5\,nl$	1.12	Savin et al. (1999, 2002a)
Fe^{10+}	$3s^2\,3p^4$	$3s^2\,3p^3\,3d\,nl$	2.00	Lestinsky et al. (2009)
		F- and Cl-like		
Fe^{17+}	$2s^2\,2p^5$	$2s\,2p^6\,nl$	0.95	Savin et al. (1997, 1999)
Fe^{9+}	$3s^2\,3p^5$	$3s^2\,3p^4\,3d\,nl$	1.44	Lestinsky et al. (2009)
		Ar-like		
Fe^{8+}	$3s^2\,3p^6$	$3s^2\,3p^5\,3d\,nl$	1.16	Schmidt et al. (2008)
Ti^{4+}	$3s^2\,3p^6$	$3s^2\,3p^5\,3d,\,nl$	1.42	Nikolić et al. (2009)
		K-like		
Fe^{7+}	$3s^2\,3p^6\,3d$	$3s^2\,3p^5\,3d^2\,nl$	1.37	Schmidt et al. (2008)

Note. Results are given only for those systems where either the authors provided enough information in their paper to determine κ or for which the original theoretical and experimental data were readily available.

We have been unable to identify any experimental explanation for the observed discrepancies. Consistent results were found by different groups using different storage rings and independently developed data reduction software. Obvious experimental issues have also been ruled out. The electron density varies across the ion beam on a much smaller scale than the effect seen here. Field ionization of the recombined ions before detection has been investigated by Schippers et al. (2001) and is believed to be well understood. Additionally, collisions of the recombined ions with electrons or background gas are predicted to be insignificant. Clearly, further experimental work is needed to flesh out the pattern which is hinted at by the data summarized above.

8. PLASMA DR RATE COEFFICIENTS

8.1. Mg^{6+}

The measured MBRRC for Mg^{6+} comprises signal from ions in the ground state as well as in various metastable states.

Because we are unable to disentangle with any confidence the ground state data from the metastable data we refrain from deriving a ground state PRRC from the measured data.

8.2. Mg^{7+}

The situation is much better for Mg^{7+}. The measured MBRRC signal is due to $\approx$97% $^2P^o_{1/2}$ ground state ions and $\approx$3% $^2P^o_{3/2}$ metastable ions. To derive a PRRC from our data, we assume all of the ions are in the ground state. The difference between the theoretical PRRC for the ground and metastable ions is less than 10% at temperatures relevant for Mg^{7+} in either photoionized or collisionally ionized gas (Badnell et al. 2003). Thus, our simplification is estimated to introduce less than an 0.3% error of the derived PRRC.

We derive the PRRC from our experimental MBRRC following the method laid out in detail in Schmidt et al. (2006) and Lestinsky et al. (2009). As was done in those works,
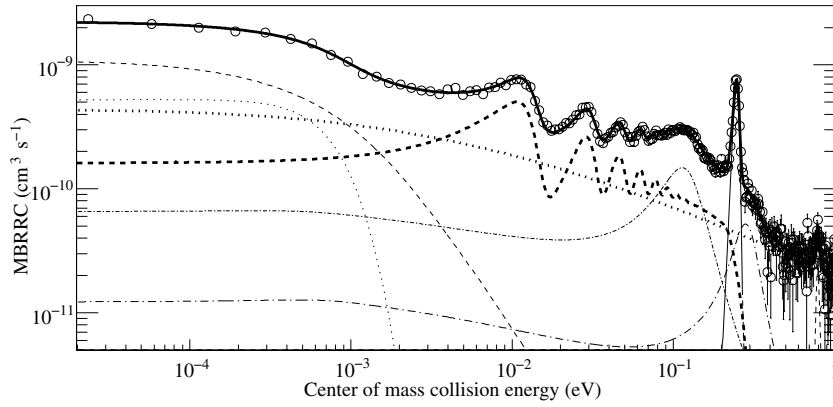
Figure 6. Mg^{7+} fit analysis for the low-energy spectrum. Circle symbols (○) with error bars show the high-expansion experimental data from Figure 5 and the solid thick curve (——) shows the model MBRRC derived from fitting Equation (9) to the data. The model MBRRC is the sum of the several components. The RR component is shown with a thick dotted line (. . .). We emulate the effects of low-energy rate enhancement with two fictitious DR resonances, which are shown using the thin short-dashed (– – –, ≲0.01 eV) and thin dotted curves (. . ., <0.002 eV). The $^2P^o_{3/2}$ Rydberg series is shown with a thick dashed curve (**- - -**). For the ^2D series with capture into $5l$, three structures were identified. Two are unresolved, broad features and are modeled using Lorentzian line shapes. The third is reproduced using a δ-like resonance. The three are respectively shown using a short dash-dotted curve (–·–), a long dash-dotted curve (–·–·), and a dash-triple dotted curve (–···, between 0.2 and 0.3 eV).

we split our MBRRC data into two segments: a low-energy portion up to 0.9 eV and a high-energy portion above this point. These are then individually corrected and converted to a experimentally derived DR PRRC $\alpha_P(T)$ as described below.

Above 0.9 eV we subtract the theoretical RR MBRRC from the experimental RR+DR MBRRC spectrum to obtain a pure DR spectrum $\alpha^{DR}_{hi}(E_k)$. The RR MBRRC is calculated using σ^{RR} as is described in Section 5

For energies above 0.9 eV the experimental DR resonance widths are much smaller than the resonance energy and we can approximate the cross section as

$$\sigma_{hi}(E_k) = \alpha^{DR}_{hi}(E_k) \times \left(\frac{m_e}{2E_k}\right)^{1/2}. \quad (7)$$

Field ionization in the experiment limits the nl levels detected. To account for this missing signal we use the theoretical AUTOSTRUCTURE calculations for $n \to 1000$ and subtract from that the theoretical data corrected for field ionization following the procedure of Schippers et al. (2001). We then multiply the difference $\hat{\sigma}_{hi}$ by $\hat{\kappa}^{-1} = 1/1.58$, which is the mean of the κ values in the field-ionization-affected energy ranges of 27–30, 30–37, and 37–40 eV (see Table 5). Using

$$\sigma'_{hi} = \sigma_{hi} + \hat{\sigma}_{hi}\hat{\kappa}^{-1} \quad (8)$$

corrects the experimental data for the missing high-n Rydberg levels. Although there is an estimated 18% uncertainty in the value used for $\hat{\kappa}$, the contribution of $\hat{\sigma}_{hi}\hat{\kappa}^{-1}$ to the total PRRC is only ≈10%. So the total error introduced is only ≈2%.

At low energies, the measured DR resonance widths are comparable to the resonance energies and the approximation of Equation (7) is no longer valid. For these energies we need to fit the data and extract resonance strengths S_r and energies E_r. This allows us to create a semi-empirical model cross section spectrum $\sigma_{lo}(E_k)$ which can later be convolved with a thermal Maxwellian electron energy distribution to derive the low-energy portion of the PRRC (Schippers et al. 2001).

To derive $\sigma_{lo}(E_k)$ we use the high-resolution data shown in Figure 5. We express $\sigma_{lo}(E_k)$ as

$$\sigma_{lo}(E_k) = \sigma^{RR}(E_k) + \sigma^{RE}(E_k) + \sigma^{DR}_{2D}(E_k) + \sigma^{DR,fi}_{2P^o_{3/2}}(E_k), \quad (9)$$

with σ^{RR} the cross section for RR, σ^{RE} the apparent cross section due to the rate enhancement effect in electron–ion merged beam experiments at low energies, σ^{DR}_{2D} the DR cross section contribution due to the ^2D core excitation, and $\sigma^{DR,fi}_{2P^o_{3/2}}$ the DR cross section contribution due to the $^2P_{3/2}$ core excitation. The cross section σ_{lo} is transformed to a model MBRRC $\alpha_m(E_k) = \langle v\sigma_{lo}(E_k)\rangle$ by convolution with the experimental electron energy distribution. This MBRRC is then fitted to the measured data. The transverse and longitudinal temperatures of the electron beam are adjusted in the fit. The same pair of temperatures is used for all components in the fit. Figure 6 gives the results of the fitting procedure for each component.

The RR cross section σ_{RR} was calculated using a hydrogenic approximation (Hoffknecht et al. 2001). That analytic formulation can be calculated significantly faster than the numerical method described in Section 2. The two approaches agree to within 0.3% within the fitted energy range. This allows for a more rapid iteration to an acceptable fit of the MBRRC data.

The rate enhancement $\sigma^{RE}(E_k)$, discussed in Section 6, was arbitrarily modeled using two near-zero DR resonances below 1 meV with fitted peak energies, widths, and resonance strengths (Lestinsky et al. 2009). These fictitious peaks have been included only so as to remove the near-zero rate enhancement factor and are not included when we calculate the experimentally derived DR PRRC.

The $2s\,2p^2\,^2D\,nl$ resonances in our data at ∼0.12–0.4 eV have been fitted using one delta function resonance and two Lorentzian-shaped resonances. The resulting peak energies, resonance strengths, and line widths are used to generate $\sigma^{DR}_{2D}(E_k)$.

The low-energy $2s^2\,2p\,^2P^o_{3/2}\,nl$ Rydberg series was fitted using AUTOSTRUCTURE calculations as a guide. The theoretical cross section was corrected by the calculated (n, l)-specific detection probabilities due to field ionization (Schippers et al. 2001). The modified theory was varied by uniformly scaling
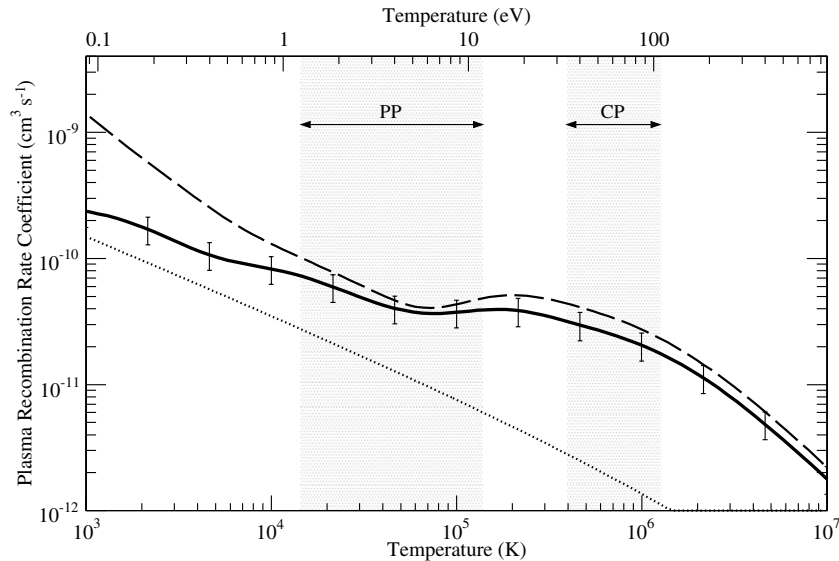
Figure 7. Mg^{7+} to Mg^{6+} DR PRRC shown for both our experimentally derived results (solid curve) and MCBP calculations (dashed curve). The error bars present the experimental uncertainties at a 90% confidence level. The dotted curve shows the RR calculations of Badnell (2006b). The shaded areas indicate the temperature regimes where Mg^{7+} is abundant ($\geqslant$1%) in either photoionized plasmas (PP; Kallman & Bautista 2001) or collisionally ionized plasmas (CP; Bryans et al. 2009).

all the resonance strengths and uniformly shifting all the resonance energies to generate the best fit cross section $\sigma^{\mathrm{DR,fi}}_{2P^o_{3/2}}(E_k)$. The fit yields only marginal corrections to the theoretical data and gives a strength factor of 0.978(2) and an energy shift of +1.3(2) meV. In order to calculate the PRRC, we re-ran the AUTOSTRUCTURE calculations for this Rydberg series but without the field-ionization modifications and adjusted the results using the strength and energy corrections from our fit to generate $\sigma^{\mathrm{DR},n\to 1000}_{2P^o_{3/2}}$.

We then constructed the total DR cross section σ^{DR} from the contributions discussed above giving

$$\sigma^{\mathrm{DR}} = \sigma^{\mathrm{DR}}_{2D} + \sigma^{\mathrm{DR},n\to 1000}_{2P^o_{3/2}} + \sigma'_{\mathrm{hi}}. \tag{10}$$

The total experimentally derived DR PRRC for Mg^{7+} $\alpha_{\mathrm{P}}(T_e)$ is obtained by multiplying Equation (10) by the relative collision velocity and convolving the product with an isotropic Maxwellian electron energy distribution (e.g., Schippers et al. 2004). The uncertainty in the experimentally derived PRRC is given by the quadrature sum of the total experimental uncertainties discussed in Section 5 and the uncertainties in the field-ionization correction discussed above. The error is estimated at ±27% at 400 K and ±25% for $\geqslant$800 K.

We show our experimentally derived DR PRRC in Figure 7 using a black solid curve. Also shown in this figure are the updated parameterized calculations of Badnell et al. (2003) using a dashed curve and the RR PRRC shown using a dotted curve. The temperature ranges, where Mg^{7+} is abundant in PPs or CPs, are indicated using shaded boxes.

The data of Badnell et al. (2003) lie above the experimental results over the full temperature range. As experiment and theory are in good agreement for the $^2P^o_{3/2}$ DR series, the diverging behavior toward low temperatures is most likely due to the theoretical uncertainties in the $5l$ Rydberg resonance of the ^2D series discussed in Section 6. These resonance positions are apparently not correctly predicted at small energies. As was shown by Schippers et al. (2004), small variations in DR resonance positions at very low energies can have a tremendous

Table 7
Mg^{7+} PRRC Fit Parameters c_i (cm^3 s^{-1} K$^{3/2}$) and E_i (K)

i	c_i	E_i
1	5.40(−6)	3.51(2)
2	3.54(−5)	2.25(3)
3	2.94(−4)	1.77(4)
4	3.55(−5)	4.85(4)
5	7.75(−4)	8.09(4)
6	1.14(−2)	3.10(5)
7	8.58(−3)	7.39(5)
8	4.34(−2)	1.84(6)

Note. The data format $x(y)$ used in this table is a short notation for $x \times 10^y$.

impact on the PRRC in density plasmas. In the PP temperature range we find the theoretical PRRC to be larger than that derived experimentally by 40% at kT_e = 1.25 eV, 11% at 5.6 eV, and 26% at 11.9 eV. At higher plasma electron temperatures, the marginal difference between theory and experiment most likely originates from the large differences between the theoretical and measured resonance strengths, as indicated by the $\kappa > 1$ values seen in Table 5. In the CP range, we find theory to be larger by 38% at 36 eV, 35% at 67 eV, and 30% at 125 eV.

For convenient inclusion of our experimentally derived PRRC into plasma modeling codes, we have fitted the results using the function

$$\alpha^{\mathrm{fit}}_{\mathrm{P}}(T) = T^{-3/2} \sum_i c_i \exp(-E_i/T). \tag{11}$$

The fit was performed over the temperature range of 400 K to 10^7 K. The results for c_i and E_i are given in Table 7. The difference between α_{P} and the fit is <2% between 400 and 10^5 K and is <0.5% from 10^5 to 10^7 K.

9. SUMMARY

We have presented here our experimental MBRRC for DR of Mg^{6+} via ΔN = 0 core excitations and for DR of Mg^{7+}

via $\Delta N = 0$ and $= 1$ core excitations. These ions both have metastable levels with lifetimes comparable to the ion storage time in TSR. We have developed a simple cascade model for estimating the relative population for each of the metastable levels. This analysis shows that there was a large metastable population for the stored Mg^{6+}. Only a small fraction of the stored ion beam is in the ground state. For Mg^{7+}, the metastable population is estimated to contribute about 3% on average.

Generally, our measured data show good agreement with state-of-the-art MCBP theory for most of the energies measured. However, some important differences between both data sets remain. At small relative energies, theory does a poor job of reproducing the observed resonance structure and strength. This is a well-known limitation of current theoretical techniques at low energies and can be important for modeling low-temperature plasmas (Schippers et al. 2004).

At higher energies, significant differences between theory and experiment are found for DR into $n \gtrsim 10$ and where the stabilization is primarily due to a radiative transition of the excited core electron. While the energy structure of the theoretical data agrees well with measurements, disagreement is found for the resonance strengths. These continue a trend already noted previously (Lestinsky et al. 2009). Puzzled by this pattern, we have reviewed experimental and theoretical sets of DR data obtained during the past two decades. For those ions with complex valence shells, the ratio of summed experimental and summed theoretical resonance strengths is larger than can be explained by experimental uncertainty limits. We have not been able to identify any experimental explanations for this effect. More research on this topic is clearly required.

Given the small metastable contamination of the Mg^{7+} data, we have been able to derive a ground state PRRC for plasma temperatures ranging from 400 K to 10^7 K. This rate coefficient includes DR via $2 \rightarrow 2$ and $2 \rightarrow 3$ core excitations. We have also presented a fit to our results which may readily be incorporated into plasma modeling codes.

REFERENCES

Altun, Z., Yumak, A., Badnell, N. R., Colgan, J., & Pindzola, M. S. 2004, A&A, 420, 775
Altun, Z., Yumak, A., Badnell, N. R., Colgan, J., & Pindzola, M. S. 2005, A&A, 433, 395
Badnell, N. 2011, Comput. Phys. Commun., 182, 1528
Badnell, N. R. 1986, J. Phys. B: At. Mol. Phys., 19, 3827
Badnell, N. R. 2006a, J. Phys. B: At. Mol. Opt. Phys., 39, 4825
Badnell, N. R. 2006b, ApJS, 167, 334
Badnell, N. R., O'Mullane, M. G., Summers, H. P., et al. 2003, A&A, 406, 1151
Baumann, P., Blum, M., Friedrich, A., et al. 1988, Nucl. Instrum. Methods A, 268, 531
Böhm, S., Müller, A., Schippers, S., et al. 2003, A&A, 405, 1157
Böhm, S., Müller, A., Schippers, S., et al. 2005, A&A, 437, 1151
Bryans, P., Landi, E., & Savin, D. W. 2009, ApJ, 691, 1540
Ferland, G. J. 2003, ARA&A, 41, 517
Fogle, M., Badnell, N. R., Glans, P., et al. 2005, A&A, 442, 757
Gallagher, T. F. 1994, Rydberg Atoms, Cambridge Monographs on Atomic, Molecular, and Chemical Physics 3 (Cambridge: Cambridge Univ. Press)
Grieser, M., Habs, D., von Hahn, R., et al. 1991, in Proc. 1991 IEEE Particle Accelerator Conference (APS Beam Physics), Vol. 5, 1991 May 6–9, San Francisco, CA, ed. L. Lizana & J. Chew (New York: IEEE), 2817
Gu, M. F. 2003, ApJ, 590, 1131
Gwinner, G., Hoffknecht, A., Bartsch, T., et al. 2000, Phys. Rev. Lett., 84, 4822
Hoffknecht, A., Schippers, S., Müller, A., Schwalm, D., & Wolf, A. 2001, Phys. Scr. T, 92, 402
Hörndl, M., Yoshida, S., Wolf, A., et al. 2006, Phys. Rev. A, 74, 052712
Jacobs, V. L., Davis, J., Rogerson, J. E., & Blaha, M. 1979, ApJ, 230, 627
Kallman, T. R., & Bautista, M. 2001, ApJS, 133, 221
Kallman, T. R., & Palmeri, P. 2007, Rev. Mod. Phys., 79, 79
Kilgus, G., Habs, D., Schwalm, D., et al. 1992, Phys. Rev. A, 49, 5730
Lampert, A., Wolf, A., Habs, D., et al. 1996, Phys. Rev. A, 53, 1413
Lestinsky, M., Badnell, N. R., Bernhardt, D., et al. 2009, ApJ, 698, 648
Lestinsky, M., Lindroth, E., Orlov, D. A., et al. 2008, Phys. Rev. Lett., 100, 033001
Linkemann, J. 1995, PhD thesis, Univ. Stuttgart
Linkemann, J., Kenntner, J., Müller, A., et al. 1995, Nucl. Instrum. Methods B, 98, 154
Lukić, D. V., Schnell, M., Savin, D. W., et al. 2007, ApJ, 664, 1244
Martinson, I., & Gaupp, A. 1974, Phys. Rep., 15, 113
Marxer, H., & Spruch, L. 1991, Phys. Rev. A, 43, 1268
Miersch, G., Habs, D., Kenntner, J., Schwalm, D., & Wolf, A. 1996, Nucl. Instrum. Methods A, 369, 277
Mohamed, T., Nikolić, D., Lindroth, E., et al. 2002, Phys. Rev. A, 66, 022719
Müller, A. 2008, Adv. At. Mol. Opt. Phys., 55, 293
Nikolić, D., Gorczyca, T. W., & Badnell, N. R. 2009, Phys. Rev. A, 79, 012703
Novotný, O., Badnell, N. R., Bernhardt, D., et al. 2012, ApJ, 753, 57
Orban, I., Altun, Z., Källberg, A., et al. 2009a, A&A, 498, 909
Orban, I., Böhm, S., Loch, S. D., & Schuch, R. 2008, A&A, 489, 829
Orban, I., Böhm, S., & Schuch, R. 2009b, ApJ, 694, 354
Orban, I., Glans, P., Altun, Z., et al. 2006, A&A, 459, 291
Orban, I., Loch, S. D., Böhm, S., & Schuch, R. 2010, ApJ, 721, 1603
Orlov, D. A., Sprenger, F., Lestinsky, M., et al. 2005, J. Phys.: Conf. Ser., 4, 290
Pastuszka, S., Schramm, U., Grieser, M., et al. 1996, Nucl. Instrum. Methods A, 369, 11
Poth, H. 1990, Phys. Rep., 196, 135
Ralchenko, Y., Kramida, A., Reader, J., & NIST ASD Team, 2008, NIST Atomic Spectra Database, version 3.1.5 (Gaithersburg, MD: National Institute of Standards and Technology)
Savin, D. W., Bartsch, T., Chen, M. H., et al. 1997, 489, L115
Savin, D. W., Behar, E., Kahn, S. M., et al. 2002a, ApJS, 138, 337
Savin, D. W., Gwinner, G., Grieser, M., et al. 2006, ApJ, 642, 1275
Savin, D. W., Kahn, S. M., Gwinner, G., et al. 2003, ApJS, 147, 421
Savin, D. W., Kahn, S. M., Linkemann, J., et al. 1999, ApJS, 123, 687
Savin, D. W., Kahn, S. M., Linkemann, J., et al. 2002b, ApJ, 576, 1098
Schippers, S. 2009, J. Phys.: Conf. Ser., 163, 012001
Schippers, S., Bartsch, T., Brandau, C., et al. 1998, J. Phys. B: At. Mol. Opt. Phys., 31, 4873
Schippers, S., Bernhardt, D., Müller, A., et al. 2011, Phys. Rev. A, 83, 012711
Schippers, S., Lestinsky, M., Müller, A., et al. 2010, Int. Rev. At. Mol. Phys., 1, 109
Schippers, S., Müller, A., Gwinner, G., et al. 2001, ApJ, 555, 1027
Schippers, S., Schnell, M., Brandau, C., et al. 2004, A&A, 421, 1185
Schmidt, E. W., Bernhardt, D., Müller, A., et al. 2007, Phys. Rev. A, 76, 032717
Schmidt, E. W., Schippers, S., Bernhardt, D., et al. 2008, A&A, 492, 265
Schmidt, E. W., Schippers, S., Müller, A., et al. 2006, ApJ, 641, L157
Shima, K., Kuno, N., Yamanouchi, M., & Tawara, H. 1992, At. Data Nucl. Data Tables, 51, 173
Sprenger, F., Lestinsky, M., Orlov, D. A., Schwalm, D., & Wolf, A. 2004, Nucl. Instrum. Methods A, 532, 298
Steck, M., Bisoffi, G., Blum, M., et al. 1990, Nucl. Instrum. Methods A, 287, 324
Stobbe, M. 1930, Ann. Phys. (Leipzig), 7, 661
Träbert, E., Hoffmann, J., Krantz, C., et al. 2009, J. Phys. B: At. Mol. Opt. Phys., 42, 025002
Uwira, O., Müller, A., Linkemann, J., et al. 1997, Hyperfine Interact., 108, 149
Wolf, A., Buhr, H., Grieser, M., et al. 2006, Hyperfine Interact., 172, 111
Wolf, A., & Gwinner, G. 2003, Hyperfine Interact., 146/147, 5
Zatsarinny, O., Gorczyca, T. W., Korista, K. T., Badnell, N. R., & Savin, D. W. 2004, A&A, 417, 1173